J. Fluid Mech. (2019), *vol.* 873, *pp.* 1090–1115.
doi:10.1017/jfm.2019.436

Onset of fully compressible convection in a rapidly rotating spherical shell

Shuang Liu[1], Zhen-Hua Wan[1,†], Rui Yan[1], Chao Sun[2] and De-Jun Sun[1,†]

[1]Department of Modern Mechanics, University of Science and Technology of China, Hefei, Anhui 230027, China

[2]Center for Combustion Energy, Key Laboratory for Thermal Science and Power Engineering of Ministry of Education, Department of Energy and Power Engineering, Tsinghua University, Beijing 100084, China

(Received 27 December 2018; revised 22 May 2019; accepted 23 May 2019)

The onset of thermal convection in a rapidly rotating spherical shell is studied by linear stability analysis based on the fully compressible Navier–Stokes equations. Compressibility is quantified by the number of density scale heights N_ρ, which measures the intensity of density stratification of the motionless, polytropic base state. The nearly adiabatic flow with polytropic index $n = 1.499 < n_a = 1.5$ is considered, where n_a is the adiabatic polytropic index. By investigating the stability of the base state with respect to the disturbance of specified wavenumber, the instability process is found to be sensitive to the Prandtl number Pr and to N_ρ. For large Pr and small N_ρ, the quasi-geostrophic columnar mode loses stability first; while for relatively small Pr a new quasi-geostrophic compressible mode is identified, which becomes unstable first under strong density stratification. The inertial mode can also occur first for relatively small Pr and a certain intensity of density stratification in the parameter range considered. Although the Rayleigh numbers Ra for the onsets of the quasi-geostrophic compressible mode and columnar mode are different by several orders of magnitude, we find that they follow very similar scaling laws with the Taylor number. The critical Ra for convection onset is found to be always positive, in contrast with previous results based on the widely used anelastic model that convection can occur at negative Ra. By evaluating the relative magnitude of the time derivative of density perturbation in the continuity equation, we show that the anelastic approximation in the present system cannot be applied in the small-Ra and large-N_ρ regime.

Key words: buoyancy-driven instability, rotating flows

1. Introduction

Rotating thermal convection in spheres and spherical shell geometries is a classical problem and has been studied extensively, due to the relevance to many geophysical and astrophysical phenomena, as well as the fundamental issues of rotating fluid dynamics. Although the convection in most applications is in the strongly nonlinear regime, it is of great interest to study flows close to convection onset, which is

† Email addresses for correspondence: wanzh@ustc.edu.cn, dsun@ustc.edu.cn

an essential prerequisite to the understanding of complex nonlinear flow behaviours (Jones, Soward & Mussa 2000; Jones, Kuzanyan & Mitchell 2009).

The Oberbeck–Boussinesq (OB) approximation is widely used in the studies of buoyancy-driven flows, which assumes that the flow is incompressible and fluid properties are constant except in the buoyancy term, where the density is linearly dependent on the temperature (Chandrasekhar 1961; Zhang & Liao 2017). The instabilities of OB convection in rapidly rotating spheres and spherical shells have been studied extensively. At large Prandtl numbers, convection occurs in the form of slowly drifting, quasi-geostrophic columnar rolls with small horizontal length scales. Roberts (1968) and Busse (1970) proposed an asymptotic solution for this convective instability. While the convection structure is properly characterized by the Roberts–Busse theory, the critical parameters cannot be predicted accurately (Zhang 1992). Later the Roberts–Busse theory was further improved and the theoretical prediction is in a good agreement with numerical computation (Yano 1992; Jones *et al.* 2000; Dormy *et al.* 2004). The spiralling nature of columnar rolls was observed at relatively small Prandtl numbers (Busse & Hood 1982; Zhang 1992), which plays an important role in the generation of zonal flows by Reynolds stress (Jones, Rotvig & Abdulrahman 2003; Rotvig & Jones 2006). At small Prandtl numbers, relatively high-frequency inertial convection occurs first, which primarily takes place in the equatorial region (Zhang & Busse 1987; Zhang 1994, 1995; Busse & Simitev 2004). Recently, the rotating convection at even smaller Prandtl numbers was explored. Axisymmetric (torsional) modes of convection were found to dominate the convective instability at high Taylor numbers in the zero-Prandtl-number limit (Sánchez, Garcia & Net 2016*a*; Zhang, Lam & Kong 2017).

Many convection phenomena in planetary and stellar systems occur under strong density stratification (Guillot 1999*a*,*b*). Compressibility must be taken into account appropriately in modelling these systems (Spiegel & Veronis 1960). Compared with the fully compressible equations, it is often preferred to employ sound-proof approaches for saving computational costs, which have been widely utilized in the study of stratified flows (Drew, Jones & Zhang 1995; Busse, Zhang & Liao 2005; Jones *et al.* 2009, 2011; Brown, Vasil & Zweibel 2012; Lund & Fritts 2012). In these simplified models, density variations due to compressibility are retained, while acoustic waves, which are often dynamically unimportant to convection, are filtered. The anelastic approximation is one of the most widely used sound-proof approaches (Batchelor 1953; Ogura & Phillips 1962; Gilman & Glatzmaier 1981; Jones, Roberts & Galloway 1990; Braginsky & Roberts 1995; Verhoeven, Wiesehöfer & Stellmach 2015), and has been employed extensively in the study of rotating compressible convection. Based on a linear, anelastic model, Glatzmaier & Gilman (1981*a*) systematically studied the rotating compressible convection in a spherical shell and observed the enhancement of convective velocity near the outer boundary under strong density stratification. Glatzmaier & Gilman (1981*b*) further investigated the effects of viscosity, conductivity, boundary conditions and convection zone depth on the stability and structure of rotating compressible convection. Within the anelastic approximation, Drew *et al.* (1995) found that compressible convection in a rotating spherical shell can occur at negative Rayleigh numbers for large Taylor numbers and small Prandtl numbers. Considering entropy diffusion rather than thermal diffusion in the anelastic model, Jones *et al.* (2009) showed rigorously that the critical Rayleigh number for convection onset is always positive.

Given the broad usage of sound-proof approaches, it is vital to estimate the appropriateness of these simplified models in different flow systems. Recently, the

applicability of the anelastic approximation in compressible convection systems has received a lot of attention (Berkoff, Kersale & Tobias 2010; Lecoanet *et al.* 2014; Calkins, Julien & Marti 2015*a*,*b*; Verhoeven *et al.* 2015; Verhoeven & Glatzmaier 2018). Calkins *et al.* (2015*b*) studied the linear stability of compressible convection in a plane layer geometry with Prandtl number $Pr = 1$. They considered the flows with/without rotation, and the results of fully compressible equations and anelastic approximation were compared, showing that the critical parameters of convection onset based on the fully compressible equations approach those of anelastic equations in the adiabatic limit. Calkins *et al.* (2015*a*) investigated the instability of rotating compressible convection in a similar plane layer geometry at lower Prandtl numbers. The anelastic approximation was found to fail in the rapidly rotating and small-Prandtl-number regime. Verhoeven & Glatzmaier (2018) further studied the validity of sound-proof approaches of rotating compressible convection in a plane layer geometry. The failure of the anelastic model for marginally stable convection was confirmed, and the conditions for a safe application were clarified. Besides, by some numerical test cases, it was shown that the anelastic model works well for both the supercritical linear convection and fully nonlinear turbulent convection for the parameters they considered.

So far, although the compressible convection in rotating spherical shells has been studied extensively based on anelastic models, the relevant study based on the fully compressible equations has not been reported to the best of our knowledge, and the applicability of the anelastic approximation in such a convection system still needs to be clarified. Thus, this study is devoted to investigating the stability characteristics of compressible convection in a rapidly rotating spherical shell using linear stability analysis based on the fully compressible equations, and the applicability of the anelastic approximation is also evaluated quantitatively. It is found that the stability characteristics of the motionless base state are sensitive to the Prandtl number and the intensity of density stratification. For relatively small Prandtl number and strong density stratification, a new quasi-geostrophic compressible mode is identified which loses stability first, resulting in a sharp decrease of critical Rayleigh number of convection onset. By evaluating the relative magnitude of the time derivative of density perturbation in the continuity equation, it is found that the anelastic approximation in the present system cannot be applied in the regime of small Rayleigh number and strong density stratification.

The remainder of this paper is organized as follows. The model is described in detail in § 2, including the governing equations and numerical approaches for linear stability analysis. In § 3 the stability characteristics of rotating compressible convection are presented, and then the validity of the anelastic approximation is discussed in § 4. Finally, we summarize our findings in § 5.

2. Model description

We consider a spherical shell rotating uniformly with a constant angular frequency $\boldsymbol{\Omega}$, as shown in figure 1. The flow region is confined between two spheres with radii r_i and r_o, with radius difference $d = r_o - r_i$ and radius ratio $\eta = r_i/r_o$. The subscripts i and o indicate quantities at the inner and outer boundaries, respectively. The working fluid is a perfect gas, and the dynamic viscosity μ and thermal conductivity k are assumed to be constant. Considering the gravitational force due to the inner core with effective mass M, the gravity field is $\boldsymbol{g}(r) = -GM\boldsymbol{r}/r^3$ within the shell, where G is the gravitational constant and $\boldsymbol{r}$ the position vector. In the rotating coordinate

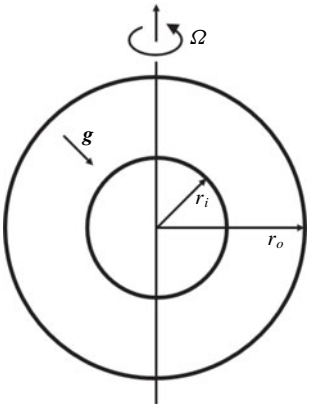

FIGURE 1. Schematic of rotating spherical shell.

system, assuming the centrifugal force is negligible compared with the gravitational force, the velocity vector $\boldsymbol{u}$, density ρ, temperature T and pressure p satisfy the fully compressible Navier–Stokes equations, which read

$$\left.\begin{gathered}\frac{\partial \rho}{\partial t}+\boldsymbol{\nabla}\cdot(\rho\boldsymbol{u})=0,\\ \rho\left(\frac{\mathrm{D}\boldsymbol{u}}{\mathrm{D}t}+2\boldsymbol{\Omega}\times\boldsymbol{u}\right)+\boldsymbol{\nabla}p-\rho\boldsymbol{g}=\mu\left[\nabla^2\boldsymbol{u}+\frac{1}{3}\boldsymbol{\nabla}(\boldsymbol{\nabla}\cdot\boldsymbol{u})\right],\\ \rho c_v\frac{\mathrm{D}T}{\mathrm{D}t}+p\boldsymbol{\nabla}\cdot\boldsymbol{u}=k\nabla^2T+\mu\Phi,\\ (c_p-c_v)\rho T=p,\end{gathered}\right\} \tag{2.1}$$

where c_p and c_v are the specific heats at constant pressure and volume, respectively. The ratio of the specific heats $\gamma=c_p/c_v$ is fixed at 5/3 in this study, representing a monoatomic ideal gas. Viscous heating is $\mu\Phi$ with

$$\Phi=\frac{\partial u_i}{\partial x_j}\left(\frac{\partial u_i}{\partial x_j}+\frac{\partial u_j}{\partial x_i}-\frac{2}{3}\delta_{ij}\boldsymbol{\nabla}\cdot\boldsymbol{u}\right). \tag{2.2}$$

Equations (2.1) are complemented by a free-slip condition for the velocity $\boldsymbol{u}$ and an isothermal condition for the temperature T at the inner and outer boundaries. In this study, no heat sources are considered inside the shell, and convection is driven by the buoyancy force due to the entropy difference between the inner and outer boundaries.

We consider a polytropic base state without convection, which is in thermal and static equilibrium, satisfying (Drew *et al.* 1995)

$$\nabla^2\overline{T}=0,\quad \boldsymbol{\nabla}\overline{p}=\overline{\rho}\boldsymbol{g},\quad \overline{p}\sim\overline{\rho}^{1+1/n}, \tag{2.3a–c}$$

where n is the polytropic index. The quantities of the base state are indicated by overbars. Based on (2.3), we obtain the base state

$$\overline{T}=\overline{T}_c\lambda(r),\quad \overline{\rho}=\overline{\rho}_c\lambda(r)^n,\quad \overline{p}=\overline{p}_c\lambda(r)^{n+1}, \tag{2.4a–c}$$

where the subscript c indicates quantities at the midpoint $r_c = (r_o + r_i)/2$, and

$$n = \frac{GM}{(c_p - c_v)\overline{T}_c \lambda_b d} - 1, \quad \lambda(r) = \lambda_a + \lambda_b \frac{d}{r}. \tag{2.5a,b}$$

Here,

$$\lambda_a = \frac{2\lambda_o - \eta - 1}{1 - \eta}, \quad \lambda_b = \frac{(1+\eta)(1-\lambda_o)}{(1-\eta)^2}, \tag{2.6a,b}$$

where $\lambda_o = \lambda(r_o)$. The intensity of density stratification can be quantified by the number of density scale heights $N_\rho = \ln(\overline{\rho}_i/\overline{\rho}_o)$, which is related to parameters (η, n, λ_o) by

$$\lambda_o = \frac{\eta + 1}{\eta \mathrm{e}^{N_\rho/n} + 1}. \tag{2.7}$$

Both λ_o and N_ρ can be used to measure compressibility (Glatzmaier & Gilman 1981*a*; Drew *et al.* 1995). In the OB limit, $\lambda_o \to 1$ and $N_\rho \to 0$, while in the high-compressibility limit, $\lambda_o \to 0$ and $N_\rho \to \infty$.

The entropy of the base state is $\overline{s} = c_p((1/\gamma)\ln\overline{p} - \ln\overline{\rho})$. The entropy difference between the inner and outer boundaries is

$$\Delta\overline{s} = \overline{s}_i - \overline{s}_o = c_p N_\rho \frac{n + 1 - n\gamma}{n\gamma}. \tag{2.8}$$

For isentropic (adiabatic) flows with non-vanishing density stratification, the (adiabatic) polytropic index $n_a = 1/(\gamma - 1) = 1.5$.

The dynamics of infinitesimal disturbances $(\rho', T', p', \boldsymbol{u}')$ superimposed on the base state is governed by the linearized equations

$$\left.\begin{gathered} \frac{\partial \rho'}{\partial t} + \boldsymbol{\nabla}\cdot(\lambda^n \boldsymbol{u}') = 0, \\ \lambda^n \frac{\partial \boldsymbol{u}'}{\partial t} + \sqrt{\frac{Pr\,Ta}{Ra}}\lambda^n \hat{\boldsymbol{z}} \times \boldsymbol{u}' + \frac{\boldsymbol{\nabla} p'}{\epsilon} + \frac{\rho' \boldsymbol{r}}{\epsilon(1-\eta)^2 r^3} = \sqrt{\frac{Pr}{Ra}}\left[\nabla^2 \boldsymbol{u}' + \frac{1}{3}\boldsymbol{\nabla}(\boldsymbol{\nabla}\cdot\boldsymbol{u}')\right], \\ \lambda^n \frac{\partial T'}{\partial t} + \lambda^n \boldsymbol{u}'\cdot\boldsymbol{\nabla}\lambda + (\gamma - 1)\lambda^{n+1}\boldsymbol{\nabla}\cdot\boldsymbol{u}' = \frac{\gamma}{\sqrt{Pr\,Ra}}\nabla^2 T', \\ \lambda_b(n+1)(1-\eta)^2 p' = \lambda^n T' + \lambda \rho'. \end{gathered}\right\} \tag{2.9}$$

Here, $\hat{\boldsymbol{z}}$ is the unit vector directed along the rotation axis. Equations (2.9) are non-dimensionalized using radius difference d, free-fall velocity $U = \sqrt{\Delta\overline{s} g_o d/c_p}$, reference time d/U, reference density $\overline{\rho}_c$, reference temperature $\overline{T}_c$, reference pressure $\overline{\rho}_c g_o d$ and reference entropy c_p, where $g_o = |\boldsymbol{g}(r_o)|$. The reference values of kinematic viscosity and thermal diffusivity are $\nu_c = \mu/\overline{\rho}_c$ and $\kappa_c = k/(c_p\overline{\rho}_c)$, respectively. For simplicity, the superscript $(\cdot)'$ of disturbances are omitted in the following discussion.

The three dimensionless control parameters in the governing equations are the Rayleigh number Ra, the Prandtl number Pr and the Taylor number Ta, which are defined as

$$Ra = \frac{g_o d^3 \Delta\overline{s}}{\kappa_c \nu_c c_p}, \quad Pr = \frac{\nu_c}{\kappa_c}, \quad Ta = \left(\frac{2\Omega d^2}{\nu_c}\right)^2. \tag{2.10a–c}$$

Besides, there is a geometric parameter, i.e. the radius ratio $\eta = r_i/r_o$. The dimensionless entropy difference ϵ is related to N_ρ and n as

$$\epsilon \equiv \frac{\Delta \bar{s}}{c_p} = \frac{N_\rho(n+1-n\gamma)}{n\gamma}. \tag{2.11}$$

For adiabatic flows, we have $\epsilon = 0$ and $n = n_a$ ($n_a = 1.5$). Convection occurs in the superadiabatic regime in the sense that $\epsilon > 0$ and $n < n_a$.

We employ a spherical coordinate system (r, θ, ϕ), where r, θ and ϕ indicate radius, colatitude and longitude, respectively. The velocity components along the (r, θ, ϕ) directions are (u_r, u_θ, u_ϕ). For numerical treatment it is favourable to use the horizontal velocity divergence δ and radial vorticity ζ rather than primitive variables (u_θ, u_ϕ) (Chan *et al.* 1994; Cai, Chan & Deng 2011). In terms of (u_θ, u_ϕ) the variables (δ, ζ) read

$$\left.\begin{aligned} \delta &= \left(\frac{1}{r}\frac{\partial}{\partial\theta} + \frac{\cos\theta}{r\sin\theta}\right)u_\theta + \frac{1}{r\sin\theta}\frac{\partial u_\phi}{\partial\phi}, \\ \zeta &= \left(\frac{1}{r}\frac{\partial}{\partial\theta} + \frac{\cos\theta}{r\sin\theta}\right)u_\phi - \frac{1}{r\sin\theta}\frac{\partial u_\theta}{\partial\phi}. \end{aligned}\right\} \tag{2.12}$$

Then, we rewrite (2.9) in terms of $(\rho, T, p, u_r, \delta, \zeta)$ as

$$\left.\begin{aligned} \frac{\partial\rho}{\partial t} + n\lambda^{n-1}u_r\frac{\mathrm{d}\lambda}{\mathrm{d}r} + \lambda^n\nabla\cdot\boldsymbol{u} &= 0, \\ \lambda^n\frac{\partial u_r}{\partial t} + C_r + \frac{1}{\epsilon}\frac{\partial p}{\partial r} + \frac{\rho}{\epsilon(1-\eta)^2r^2} &= \tau_r, \\ \lambda^n\frac{\partial\delta}{\partial t} + C_\delta + \frac{\nabla_H^2 p}{\epsilon} &= \tau_\delta, \\ \lambda^n\frac{\partial\zeta}{\partial t} + C_\zeta &= \tau_\zeta, \\ \lambda^n\frac{\partial T}{\partial t} + \lambda^n u_r\frac{\mathrm{d}\lambda}{\mathrm{d}r} + (\gamma-1)\lambda^{n+1}\nabla\cdot\boldsymbol{u} &= \frac{\gamma}{\sqrt{PrRa}}\nabla^2 T, \\ \lambda_b(n+1)(1-\eta)^2 p &= \lambda^n T + \lambda\rho, \end{aligned}\right\} \tag{2.13}$$

where

$$\left.\begin{aligned} \nabla\cdot\boldsymbol{u} &= \frac{1}{r^2}\frac{\partial}{\partial r}(r^2u_r) + \delta, \\ \nabla_H^2 &= \frac{1}{r^2\sin\theta}\frac{\partial}{\partial\theta}\left(\sin\theta\frac{\partial}{\partial\theta}\right) + \frac{1}{r^2\sin^2\theta}\frac{\partial^2}{\partial\phi^2}. \end{aligned}\right\} \tag{2.14}$$

The expressions of $C_{r,\delta,\zeta}$ and $\tau_{r,\delta,\zeta}$ pertaining to the Coriolis and viscous forces are given in appendix A. The terms containing u_θ or u_ϕ in (2.13) can be expressed in terms of δ and ζ, as shown in appendix B. The free-slip and isothermal boundary conditions imply that

$$u_r = \frac{\partial\delta}{\partial r} = \frac{\partial\zeta}{\partial r} = T = 0, \quad \text{at } r = r_i, r_o. \tag{2.15}$$

The equations (2.13) are solved numerically by expanding the variables $\chi = (\rho, T, p, u_r, \delta, \zeta)$ in spherical harmonics,

$$\chi(t, r, \theta, \phi) = \sum_{l=0}^{L} \sum_{m=-l}^{l} \chi_l^m(t, r) Y_l^m(\theta, \phi), \tag{2.16}$$

where L is the maximal degree of triangular truncation, m is the azimuthal wavenumber, and the coefficients χ_l^m are complex functions. The spherical harmonics are normalized as

$$Y_l^m(\theta, \phi) = \sqrt{\frac{2l+1}{2} \frac{(l-m)!}{(l+m)!}} P_l^m(\cos\theta) \exp(\mathrm{i}m\phi) \quad (l \geqslant m \geqslant 0), \tag{2.17}$$

where P_l^m are the associated Legendre functions of degree l and order m. For the linear problem in the present study, eigenmodes with different azimuthal wavenumbers are uncoupled. Besides, only non-negative wavenumbers need to be considered. Thus a sequence of uncoupled eigenproblems parametrized by wavenumber $m \geqslant 0$ can be obtained. Some useful equalities related to spherical harmonic expansion are shown in appendix B. The Chebyshev collocation method is used in the radial direction (Trefethen 2000). The eigenvalue problem resulting from numerical discretization is solved iteratively by employing shift–invert preconditioners and the Arnoldi algorithm (Sánchez *et al.* 2016*a*; Sánchez, García & Net 2016*b*).

Numerical convergence is verified for the linear stability analysis and the number of Chebyshev collocation points and triangular truncation degree L are taken so that the leading eigenvalue is computed with an accuracy of at least 10^{-4}. In the study of linear stability of rotating compressible convection in a plane layer geometry, the critical parameters based on fully compressible equations approach those based on anelastic equations in the adiabatic limit at $Pr = 1$ (Calkins *et al.* 2015*b*), while in the rapidly rotating and small-Pr regime the anelastic approximation fails (Calkins *et al.* 2015*a*; Verhoeven & Glatzmaier 2018). To assess the reliability in the numerical computation, we consider nearly adiabatic flows ($n = 1.499$) at relatively large Pr and compare the critical parameters of convection onset based on fully compressible equations with those based on anelastic equations reported in Drew *et al.* (1995), which are given in table 1. Owing to the different non-dimensional scales used, the transformations for the Rayleigh number $Ra = Ra^D N_\rho (1-\eta)^2/(\lambda_b n_a)$ and the frequency $\omega = \omega^D \sqrt{Pr/Ra}$ are employed (the superscript D indicates dimensionless variables employed by Drew *et al.* (1995)). In addition, figure 2 shows the comparison of critical eigenmodes. The results based on the two sets of equations are in good agreement, indicating the reliability of our computation.

To examine the applicability of the anelastic model for compressible convection in a rapidly rotating spherical shell, we consider nearly adiabatic flows ($n = 1.499$) under rapid rotation ($10^6 \lesssim Ta \leqslant 10^{11}$) in a fixed configuration with $\eta = 0.4$. The effects of compressibility are investigated with $0 < N_\rho \leqslant 5$. We consider Pr values where convection takes a non-axisymmetric columnar form under the OB approximation with $0.1 \lesssim Pr \leqslant 10$. In this Pr range, the breakdown of the anelastic approximation is observed for compressible convection in a rotating plane layer (Calkins *et al.* 2015*a*; Verhoeven & Glatzmaier 2018). The very small-Pr regime, where convection will be dominated by the inertial modes (Zhang 1994), has not been explored in this study. For given (Pr, Ta, N_ρ), the stability characteristics of the base state are dependent on Ra, and the critical Ra for convection onset is a function of (Pr, Ta, N_ρ).

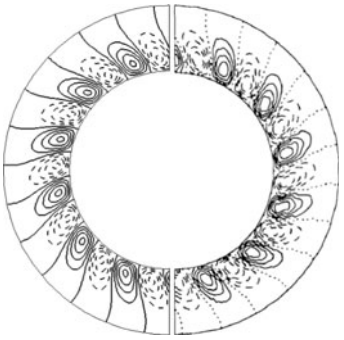

FIGURE 2. Distribution of u_r of the critical eigenmodes in the equatorial plane for the case with $(\eta, Pr, N_\rho, Ta) = (0.6, 1, 5, 10^5)$. The result on the left-hand side is based on the fully compressible equations, while that on the right-hand side is based on the anelastic equations (Drew *et al.* 1995).

	Equations	Ta	Ra_c	m_c	ω_c
Drew *et al.* (1995)	AE	10^5	7109	13	−0.5074
Present	FC	10^5	7116	13	−0.5068
Drew *et al.* (1995)	AE	3×10^4	3809	10	−0.4250
Present	FC	3×10^4	3813	10	−0.4246

TABLE 1. Comparison of critical Rayleigh numbers Ra_c, critical wavenumbers m_c and critical frequencies ω_c based on the fully compressible equations (FC) for nearly adiabatic flows ($n = 1.499$) with those based on the anelastic equations (AE) in Drew *et al.* (1995) for $(\eta, Pr, N_\rho) = (0.6, 1, 5)$.

3. Linear stability analysis

3.1. *The base state*

For a fixed configuration with $\eta = 0.4$, the motionless base state is dependent on parameters (n, N_ρ), as shown in (2.6) and (2.7). Entropy $\bar{s}$ is determined up to a constant. The entropy profiles for $N_\rho = 5$ and different n are depicted in figure 3(*a*). It shows that the base state becomes isentropic as $n \to n_a = 1.5$. Figure 3(*b*) displays the density profiles $\overline{\rho}$ for $n = 1.499$ and different N_ρ. The intensity of density stratification increases rapidly with N_ρ. For $N_\rho = 5$, the density ratio between the inner and outer boundaries reaches up to 148.

3.2. *Instability under weak density stratification*

In this section, the convection onset under weak density stratification is considered with N_ρ fixed at 0.01. We first focus on the instability of the base state with respect to the disturbance of specified wavenumber m. The corresponding critical Rayleigh number is denoted as $Ra_{c,m}$. Then, the critical Rayleigh number Ra_c of the base state with respect to general disturbances is obtained by a minimization process, namely $Ra_c = \min_m Ra_{c,m}$.

Figure 4 shows the maximal growth rate σ of the base state with respect to the disturbance of wavenumber $m = 5$ as a function of Ra for $Pr = 0.1$, $Ta = 10^8$ and

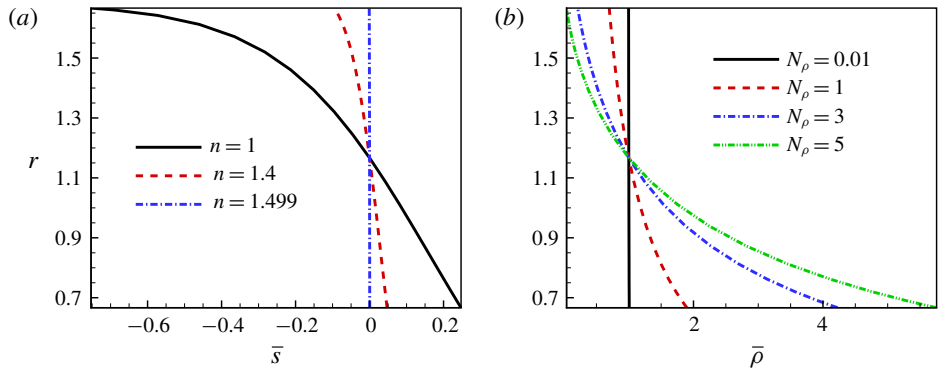

FIGURE 3. (Colour online) The base state for $\eta = 0.4$. (*a*) The distributions of entropy $\bar{s}$ for $N_\rho = 5$ and different n. As $n \to n_a = 1.5$, the base state becomes isentropic. (*b*) The distributions of density $\bar{\rho}$ for $n = 1.499$ and different N_ρ.

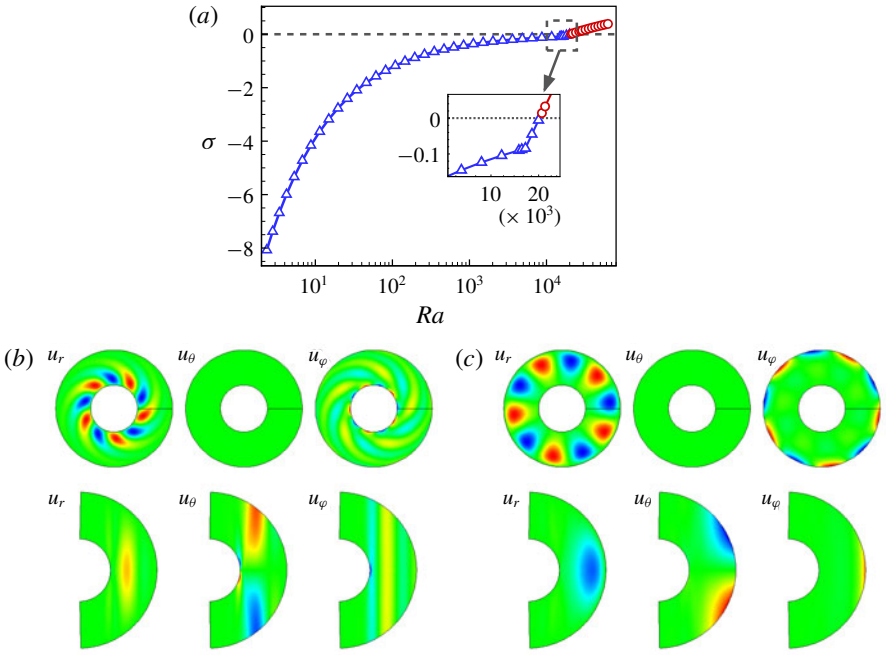

FIGURE 4. (Colour online) The maximal growth rate σ of the base state with respect to the disturbance of wavenumber $m = 5$ as a function of Ra for $Pr = 0.1$, $Ta = 10^8$ and $N_\rho = 0.01$. Negative and positive growth rates are denoted by blue triangles and red circles, respectively. The inset is an enlarged view near the instability threshold. (*b*,*c*) The two most unstable eigenmodes at $Ra = 2.81 \times 10^4$. Disturbance distributions on the equatorial and meridional planes are shown in the first and second rows, respectively. The ϕ location of the meridional section is marked by the horizontal radius. (*b*) The most unstable eigenmode with complex growth rate $0.128 - 0.531\mathrm{i}$. (*c*) The second most unstable eigenmode with complex growth rate $-0.060 - 2.40\mathrm{i}$.

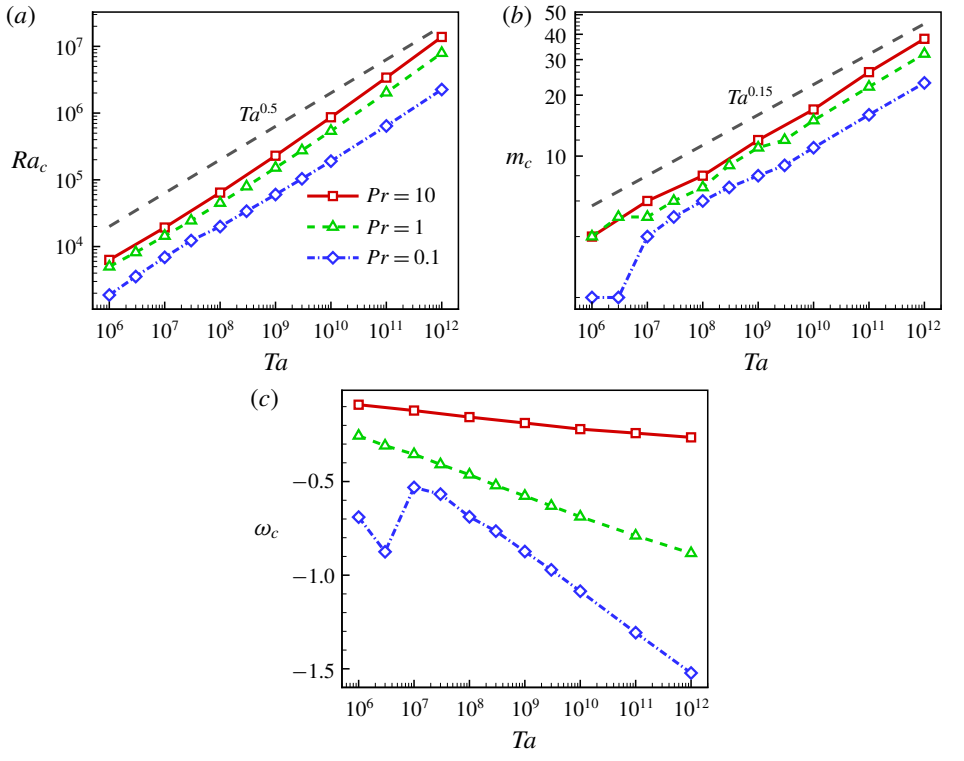

FIGURE 5. (Colour online) (*a*) Critical Rayleigh number Ra_c, (*b*) critical wavenumber m_c and (*c*) critical frequency ω_c as functions of Ta for $Pr = 10,\ 1,\ 0.1$ and $N_\rho = 0.01$.

$N_\rho = 0.01$. In this Ra range, the maximal growth rate increases monotonically with Ra. We note that in the small-Ra limit the magnitude of growth rate $|\sigma|$ decreases with Ra and satisfies a certain scaling law, which will be shown in § 4. The two most unstable eigenmodes near the instability threshold are depicted in figure 4(*b*,*c*), showing the distributions of velocity perturbations on the equatorial and meridional planes. In figure 4(*b*), the most unstable eigenmode is the typical columnar mode (Roberts 1968; Busse 1970; Zhang 1992; Zhang & Liao 2017). The columnar structure of disturbance originates from a strong Taylor–Proudman effect (Proudman 1916; Taylor 1921). In figure 4(*c*), the second most unstable eigenmode is the typical inertial mode with convection occurring in the equatorial region (Zhang 1994; Zhang & Liao 2017). Generally, at relatively large Pr, the columnar mode becomes unstable first, while the inertial mode is dominant for small Pr. Besides Pr, the type of dominant mode is also dependent on Ta.

Now, we focus on the instability of the base state with respect to general disturbances. Figure 5 gives the critical Rayleigh number $Ra_c = \min_m Ra_{c,m}$ and corresponding critical wavenumber m_c and critical frequency ω_c as functions of Ta for $Pr = 10,\ 1$ and 0.1. It is found that Ra_c, m_c and $|\omega_c|$ increase with Ta for large enough Ta. As Ta increases, the Taylor–Proudman effect is enhanced and convection is suppressed. It is also observed that Ra_c and m_c satisfy a certain power-law scaling with respect to Ta. Lines of constant slope are included as guiding lines which reasonably describe the scaling behaviours of critical parameters. It is of interest to develop the asymptotic theory of convective instability for the fully compressible

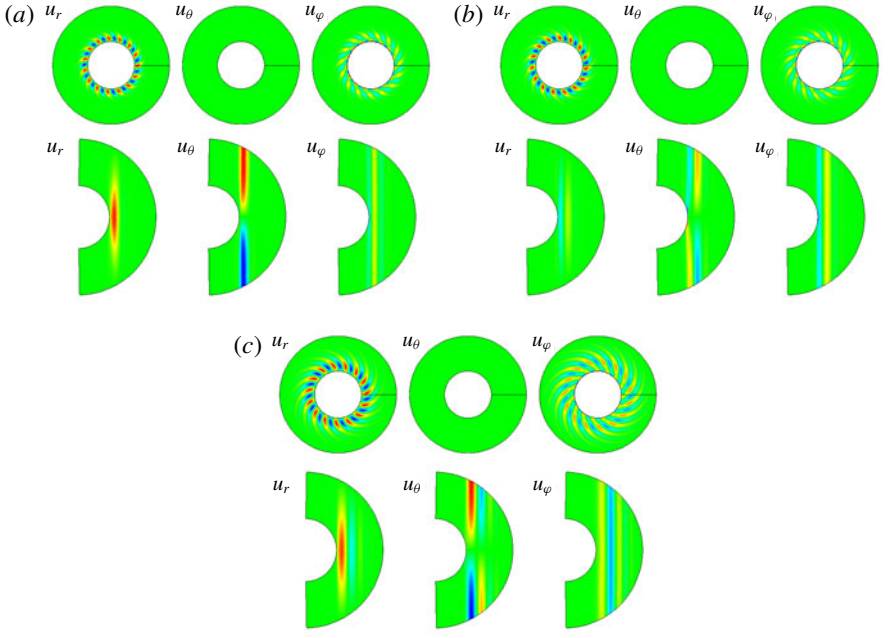

FIGURE 6. (Colour online) Critical eigenmodes with wavenumber $m = 15$ for $Pr = 10,\ 1,\ 0.1$, $Ta = 10^{10}$ and $N_\rho = 0.01$: (*a*) $Pr = 10$, $Ra_c = 8.820 \times 10^5$, $\omega_c = -0.224$; (*b*) $Pr = 1$, $Ra_c = 5.390 \times 10^5$, $\omega_c = -0.688$; (*c*) $Pr = 0.1$, $Ra_c = 2.240 \times 10^5$, $\omega_c = -0.929$.

model and compare the theoretical predictions with the numerical results, which are outside the scope of this study. With the decrease of Pr, both Ra_c and m_c decrease, while the scaling exponents of Ra_c and m_c seem to be insensitive to variation of Pr. The anomaly in the variations of critical parameters at $Pr = 0.1$ in figure 5 is due to the switching of dominant eigenmodes.

In the Pr range considered ($0.1 \lesssim Pr \leqslant 10$), the columnar mode becomes unstable first under strong rotation and weak density stratification. Considering the disturbance of wavenumber $m = 15$, the critical eigenmodes for $Pr = 10,\ 1,\ 0.1$ and $Ta = 10^{10}$ are shown in figure 6. It is found that these critical modes are quasi-geostrophic and convection is localized in the tangent cylindrical annulus of the inner core coaxial with the rotation axis. As Pr decreases, the disturbance spirally elongates in the cylindrically radial direction, which is consistent with the observations under the OB approximation (Zhang 1992). Physically, the spirally elongated structures of critical convection at small Pr are related to the radial propagation properties of topographic Rossby waves (Takehiro 2008, 2010).

3.3. *Instability under strong density stratification*

3.3.1. *Variation of growth rate*

In this section, the influence of density stratification on the instability of the base state is studied. We first focus on studying the stability characteristics of the base state with respect to the disturbance of specified wavenumber m. It is found that the instability process is sensitive to the parameters (Pr, N_ρ). Based on the variation of maximal growth rate of the base state with Ra and the structures of critical eigenmodes, we here classified the instability processes into five categories in general.

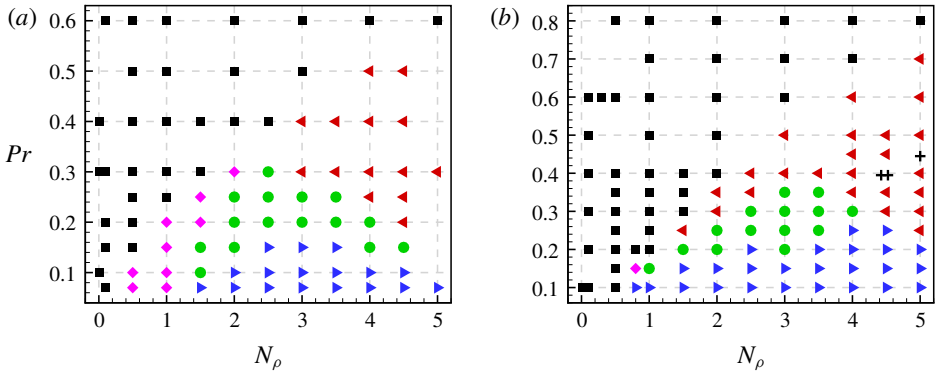

FIGURE 7. (Colour online) Phase diagrams of the instability processes of the base state in the parameter space of (Pr, N_ρ) at (a) $(Ta, m) = (10^8, 5)$ and (b) $(Ta, m) = (10^{10}, 15)$. The instability processes are classified into five major categories. Categories I to V are represented by black squares, red left-pointing triangles, purple rhombuses, green circles and blue right-pointing triangles, respectively. Note that the instability processes indicated by black crosses in (b) are more complex.

Figure 7 shows the phase diagrams of instability processes in the parameter space of (Pr, N_ρ) at $(Ta, m) = (10^8, 5)$ and $(Ta, m) = (10^{10}, 15)$. We note that the results at the two parameter combinations (Ta, m) are consistent with each other qualitatively, even though the critical parameters between different categories are different quantitatively. Therefore, we just discuss various instability processes in detail based on the results at $(Ta, m) = (10^{10}, 15)$.

The typical variations of maximal growth rate σ of the base state with Ra at different (Pr, N_ρ) are shown in figure 8, illustrating the instability processes in different categories. The structures of eigenmodes dominating different instability transitions are shown in figure 9. The instability process in the first category occurs at relatively large Pr and small N_ρ, and the columnar mode loses stability first. As an example, figure 8(a) shows the variation of σ with Ra at $(Pr, N_\rho) = (0.4, 1.5)$, while the dominant eigenmode near the instability threshold is given in figure 9(a). Compared with results under weak density stratification ($N_\rho = 0.01$), it should be mentioned that the intensification of density stratification produces a local maximum of growth rate at moderate Ra and enhances the spiral nature of the critical convection pattern. We also note that $|\sigma|$ decreases with Ra when Ra is small enough, which indicates certain scaling behaviours of the eigenpair with Ra, as will be shown in § 4.

At relatively small Pr, the maximum of the growth rate at moderate Ra increases and becomes positive as N_ρ increases. Correspondingly, a new unstable eigenmode, referred to as the quasi-geostrophic compressible mode, appears because of compressibility. Figure 8(b) shows the variation of σ with Ra at $(Pr, N_\rho) = (0.4, 4)$, corresponding to the instability process in the second category. Figure 9(b) shows the dominant eigenmodes for this instability transition. Owing to the emergence of this new unstable eigenmode, convection occurs at a much smaller Ra compared with that under weak density stratification. It is interesting that the unstable base state gains stability at higher Ra. When Ra is further increased, another instability occurs due to the unstable columnar mode. Thus, with the increase of Ra, the base state undergoes the process of 'stable → unstable → stable → unstable'. From figure 9(b), we can observe that the new unstable eigenmode for the first instability transition is

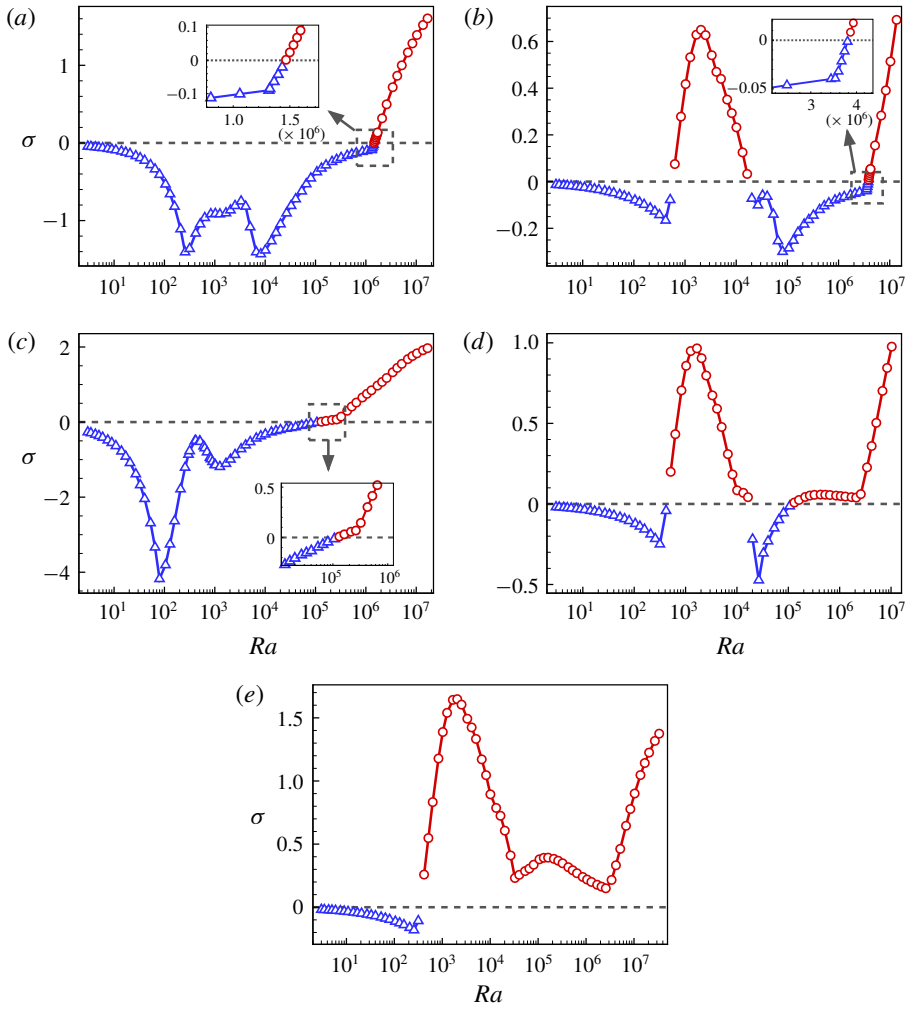

FIGURE 8. (Colour online) The maximal growth rates of the base state with respect to the disturbance of wavenumber $m = 15$ as functions of Ra at different (Pr, N_ρ), illustrating the instability processes in different categories: (*a*) $(Pr, N_\rho) = (0.4, 1.5)$, instability process in the first category; (*b*) $(Pr, N_\rho) = (0.4, 4)$, instability process in the second category; (*c*) $(Pr, N_\rho) = (0.15, 0.8)$, instability process in the third category; (*d*) $(Pr, N_\rho) = (0.3, 3)$, instability process in the fourth category; (*e*) $(Pr, N_\rho) = (0.2, 4)$, instability process in the fifth category.

quasi-geostrophic with the disturbance concentrating in the tangent cylindrical annulus of the inner core and varying weakly along the direction of rotation axis. The new mode is also characterized by small horizontal length scales. The viscous force plays an important role in the breaking of the rotational constraint for convection onset (Zhang & Liao 2017). This is reflected by the presence of Ta in the asymptotic scalings of the critical parameters, as will be shown below.

As stated in § 3.2, the columnar mode loses stability first under strong rotation and weak density stratification. For relatively small Pr, it is found that the inertial mode loses stability first under a certain intensity of density stratification. Figure 8(*c*)

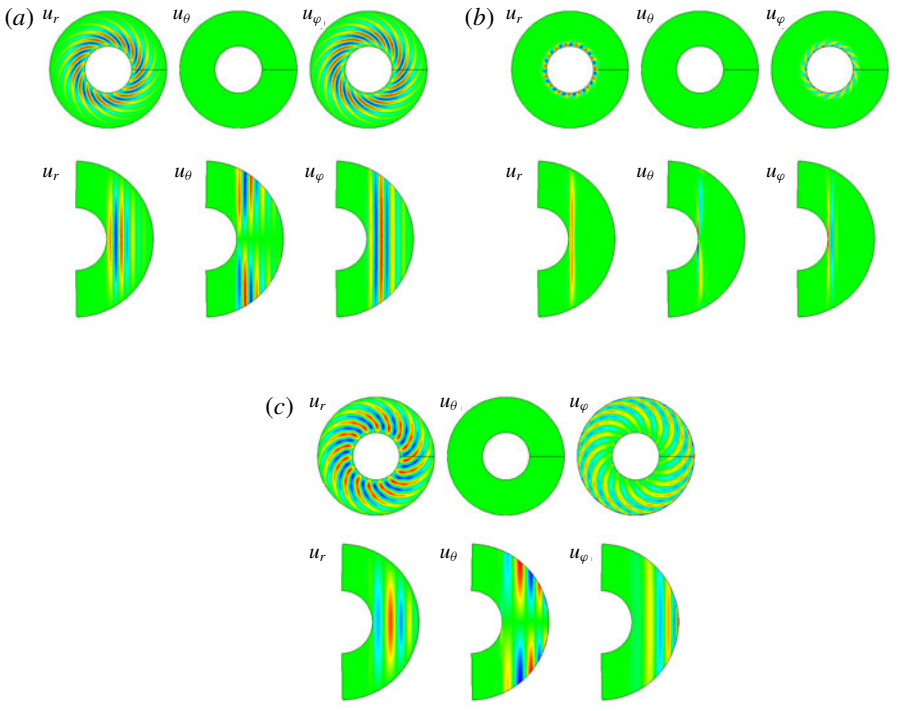

FIGURE 9. (Colour online) The dominant eigenmodes at different Ra, Pr and N_ρ. (*a*) The dominant eigenmode at $Ra = 1.46 \times 10^6$ for $(Pr, N_\rho) = (0.4, 1.5)$ with complex growth rate $0.00172 - 1.37\mathrm{i}$. (*b*) The dominant eigenmode at $Ra = 631.3$ for $(Pr, N_\rho) = (0.4, 4)$ with complex growth rate $0.0750 - 20.8\mathrm{i}$. (*c*) The dominant eigenmode at $Ra = 1.311 \times 10^5$ for $(Pr, N_\rho) = (0.15, 0.8)$ with complex growth rate $0.00935 - 4.73\mathrm{i}$.

shows the variation of maximal growth rate of the base state with Ra at $(Pr, N_\rho) = (0.15, 0.8)$, corresponding to the instability process in the third category. Figure 9(*c*) shows the dominant eigenmode for the instability transition. The quasi-geostrophic nature of the convection pattern is quite evident. By examining the distributions of various quantities, particularly u_ϕ, it is found that strong convection occurs near the equatorial region. Disturbances spirally elongate along the cylindrically radial direction and extend over a large part of the flow domain. In addition to the switching of critical eigenmode, the intensification of density stratification also gives rise to a local maximum of growth rate at moderate Ra.

At a larger N_ρ the quasi-geostrophic compressible mode becomes unstable at moderate Ra. Figure 8(*d*) shows the variation of σ with Ra at $(Pr, N_\rho) = (0.3, 3)$, corresponding to the instability process in the fourth category. Thus, as Ra increases, the base state loses stability due to the quasi-geostrophic compressible mode and gains stability at higher Ra. As Ra is further increased, another instability transition occurs, which is dominated by the inertial mode. For small Pr and a certain intensity of density stratification, the base state loses stability due to the quasi-geostrophic compressible mode and keeps being unstable at higher Ra. The variation of maximal growth rate of the base state with Ra at $(Pr, N_\rho) = (0.2, 4)$ is shown in figure 8(*e*), corresponding to the instability process in the fifth category.

At some parameter combinations (Pr, N_ρ), the instability process of the base state can be even more complicated than those mentioned before. Figure 10(*a*) shows the

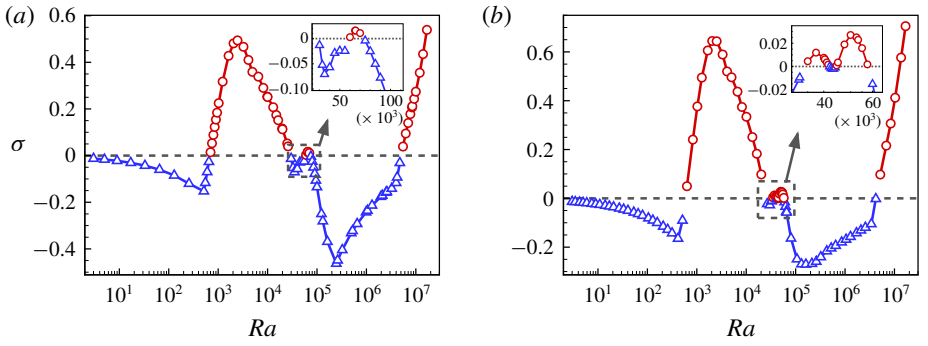

FIGURE 10. (Colour online) The maximal growth rates of the base state with respect to the disturbance of wavenumber $m = 15$ as functions of Ra at (*a*) $(Pr, N_\rho) = (0.45, 5)$ and (*b*) $(Pr, N_\rho) = (0.4, 4.5)$.

variation of maximal growth rate of the base state versus Ra at $(Pr, N_\rho) = (0.45, 5)$. As Ra increases, the base state undergoes the process of 'stable → unstable → stable → unstable → stable → unstable'. Moreover, at $(Pr, N_\rho) = (0.4, 4.5)$, the instability transition even occurs four times as Ra increases, as shown in figure 10(*b*).

For a specified eigenmode, the disturbance structure also varies significantly along with the change of growth rate. Figure 11(*a*) gives the two largest growth rates of the base state as functions of Ra. It is observed that, in a certain range of Ra, the difference between the two growth rates is evident and there is no switching of the dominant eigenmode. The structures of dominant eigenmodes at different values of Ra in this range are shown in figure 11(*b–e*). The base state loses stability due to the quasi-geostrophic compressible mode, which is shown in figure 11(*b*). Convection occurs in the neighbourhood of the tangent cylinder of the inner core. As Ra increases, disturbance elongates in the cylindrically radial direction and the spiral nature of the convection pattern becomes more evident, as shown in figure 11(*c–e*). Strong disturbances are located in the equatorial region at large Ra. The variation of disturbance structure can have an influence on the corresponding growth rate.

The instability processes discussed above occur at relatively large Ta and various (Pr, N_ρ). Next, we will investigate the stability characteristics of the base state at different Ta for specified (Pr, N_ρ), which demonstrates that the instability process also depends on Ta. Figure 12 gives the maximal growth rates of the base state with respect to the disturbance of wavenumber $m = 5$ as functions of Ra at different Ta for three parameter combinations (Pr, N_ρ). Under weak density stratification, as Ta increases, the critical Rayleigh number $Ra_{c,m=5}$ becomes larger, while the trend in the variation of the growth rate is qualitatively unchanged, as shown in figure 12(*a*). For small Pr and a certain intensity of density stratification, the variation of Ta can change qualitatively the instability process of the base state, as illustrated in figure 12(*b*,*c*). Figure 12(*b*) shows the results at $(Pr, N_\rho) = (0.1, 3)$. Starting from a small Ta, the critical Rayleigh number $Ra_{c,m=5}$ decreases rapidly as Ta is slightly increased, and the instability of the base state is promoted. However, when Ta is large enough, $Ra_{c,m=5}$ increases with Ta. Along with the change of critical Rayleigh number, the structure of the critical eigenmode also varies. We note that $Ra_{c,m=5}$ keeps being positive as Ta varies. Figure 12(*c*) shows the results at $(Pr, N_\rho) = (0.3, 5)$. At small Ta, the base state loses stability at relatively large Ra. When Ta is increased to a certain magnitude, the quasi-geostrophic compressible mode becomes unstable at much smaller Ra. Thus,

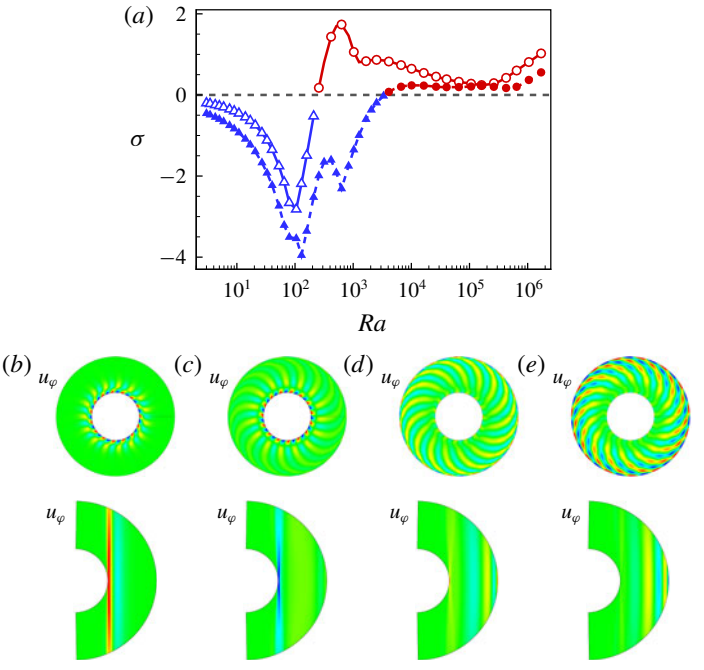

FIGURE 11. (Colour online) (*a*) The two largest growth rates of the base state with respect to the disturbance of wavenumber $m = 15$ as functions of Ra at $(Pr, N_\rho) = (0.1, 1)$. The largest and second largest growth rates are indicated by hollow and filled symbols, respectively. (*b–e*) The dominant eigenmodes at different values of Ra: (*b*) $Ra = 257$, (*c*) $Ra = 513$, (*d*) $Ra = 1025$ and (*e*) $Ra = 1.638 \times 10^4$.

with the increase of Ra, the base state undergoes the process of 'stable → unstable → stable → unstable'. The critical Rayleigh numbers for the two instability transitions increase when Ta is further increased.

It is worth mentioning that, although Ta can significantly affect the stability characteristics of the base state for some parameter combinations (Pr, N_ρ), the instability of the quasi-geostrophic compressible mode and the diversity of instability processes are still universal at large enough Ta. As also demonstrated in figure 7, the phase diagrams of the instability processes at two parameter combinations (Ta, m) are qualitatively similar. It is observed that the parameter region for the instability process in the third category is diminished for larger Ta. This is due to the fact that the instabilities of the columnar mode and quasi-geostrophic compressible mode are promoted relative to the inertial mode as Ta is increased.

3.3.2. *Variations of critical parameters*

In this section, we mainly study the instability of the base state with respect to general disturbances and calculate the critical Rayleigh number $Ra_c = \min_m Ra_{c,m}$ and corresponding wavenumber m_c and frequency ω_c. We have shown that multiple instability transitions of the base state may exist for specified parameters (Ta, m, Pr, N_ρ). For clarity, we here only consider the critical point with the smallest Ra, leaving out possible re-stability and re-instability of the base state at higher Ra.

As mentioned above, in the large-Pr regime, the instability of the base state is dominated by the columnar mode; see figure 7. Figure 13 shows the critical

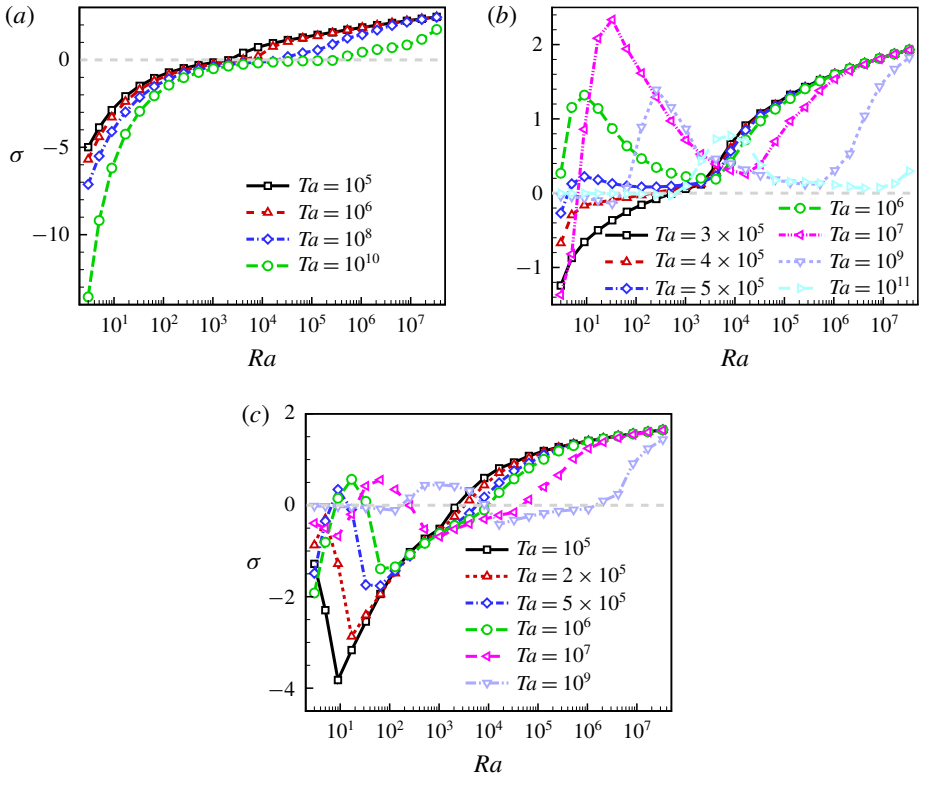

FIGURE 12. (Colour online) The maximal growth rates of the base state with respect to the disturbance of wavenumber $m = 5$ as functions of Ra at different Ta and specified (Pr, N_ρ): (*a*) $(Pr, N_\rho) = (0.1, 0.01)$, (*b*) $(Pr, N_\rho) = (0.1, 3)$ and (*c*) $(Pr, N_\rho) = (0.3, 5)$.

parameters as functions of Ta at $Pr = 10,\ 1$ and different N_ρ. We find that the trends of variations of critical parameters with Ta and N_ρ at these two Pr values are similar. As Ta increases, all of Ra_c, m_c and $|\omega_c|$ increase monotonically. More importantly, both Ra_c and m_c satisfy certain scaling laws with Ta, based on which we may extrapolate these critical parameters to higher Ta. The variation of N_ρ has only minor influences on the scaling exponents.

Figure 14 depicts the velocity distributions of critical eigenmodes on meridional planes at $Pr = 1$, $Ta = 10^{11}$ and different N_ρ, showing that convection always occurs in the neighbourhood of the tangent cylinder. The disturbances near the outer boundary are diminished as N_ρ increases, which is attributed to the constancy of dynamic viscosity μ and thermal conductivity k in our model. As N_ρ increases, the density of the base state near the outer boundary is decreased, as shown in figure 3. Then, the local kinematic viscosity $\nu = \mu/\rho$ and thermal diffusivity $\kappa = k/c_p\rho$ are increased, enhancing the diffusion effects near the outer boundary. When the thermal diffusivity κ is assumed to be constant, instead of k, convection tends to move towards the equatorial region due to compressibility (Glatzmaier & Gilman 1981*a*; Drew *et al.* 1995; Jones *et al.* 2009).

In the small-Pr regime, the instability process of the base flow is sensitive to parameters (Pr, N_ρ). When N_ρ is small, the columnar mode loses stability first, while the quasi-geostrophic compressible mode becomes unstable first under strong density

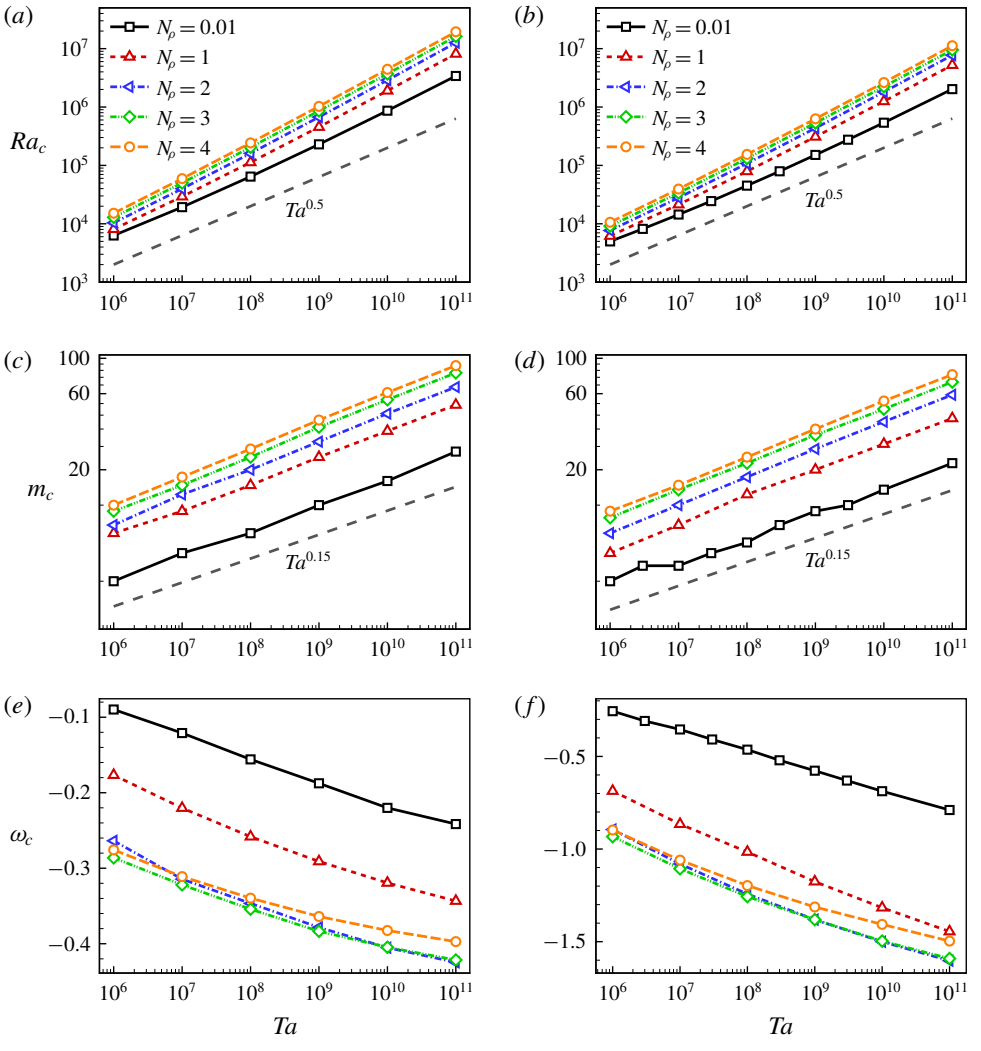

FIGURE 13. (Colour online) (*a*,*b*) Critical Rayleigh numbers Ra_c, (*c*,*d*) critical wavenumbers m_c and (*e*,*f*) critical frequencies ω_c as functions of Ta for different N_ρ at (*a*,*c*,*e*) $Pr = 10$ and (*b*,*d*,*f*) $Pr = 1$.

stratification. At some Pr, the inertial mode occurs first under density stratification of a certain intensity. The transition parameters $(Pr_c, N_{\rho,c})$ between different categories of instability process are dependent on Ta and the wavenumber m of the disturbance. For clarity, we consider only the cases with relatively weak and strong density stratification, corresponding to the critical columnar mode and quasi-geostrophic compressible mode, respectively. Figure 15 shows the variations of critical parameters with Ta at $Pr = 0.3,\ 0.1$, and figure 16 gives the maximal growth rates of the base state with respect to the disturbance of wavenumber $m = m_c(N_\rho)$ as functions of Ra at $Ta = 10^{10}$, showing the instability processes of the base state at corresponding parameters. For small N_ρ, the columnar mode occurs first. Similar to the results at larger Pr, both Ra_c and m_c satisfy certain scaling laws with Ta, and the decrease of Pr has only minor influences on the scaling exponents. At large N_ρ, the quasi-geostrophic

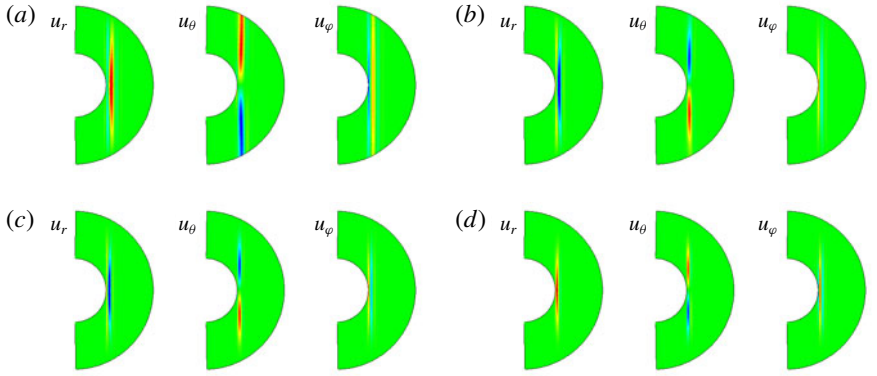

FIGURE 14. (Colour online) Velocity distributions of critical eigenmodes on meridional planes at $Pr = 1$, $Ta = 10^{11}$ and different values of N_ρ: (*a*) $N_\rho = 1$, (*b*) $N_\rho = 2$, (*c*) $N_\rho = 3$ and (*d*) $N_\rho = 4$.

compressible mode occurs first, and Ra_c decreases by several orders of magnitude. It is interesting that Ra_c of the quasi-geostrophic compressible mode satisfies a scaling law with Ta with a scaling exponent similar to that of the columnar mode. The anomalous variations of critical parameters at $(Pr, N_\rho) = (0.3, 1)$ and relatively small Ta originates from the switching of dominant eigenmodes. At $Pr = 0.1$, m_c is relatively small, and in the Ta range considered, the scaling relation between m_c and Ta is not so clear, different from that at a larger Pr.

4. Validity of anelastic approximation

Within the anelastic approximation, Drew *et al.* (1995) investigated the compressible convection in a rotating spherical shell and found that convection can occur at negative Ra for large (Ta, N_ρ) and small Pr. In contrast, based on the fully compressible equations, we find that the critical Rayleigh number is always positive in a similar parameter space, implying the inapplicability of the anelastic approximation, although the flow considered is nearly adiabatic with $n = 1.499 < n_a = 1.5$. Considering that the time derivative of density perturbation in the continuity equation is neglected under the anelastic approximation, the applicability of the anelastic model can be evaluated to some extent by measuring the relative magnitude of the time derivative of density perturbation (denoted as ξ) (Calkins *et al.* 2015*a*). The complete continuity equation reads

$$\frac{\partial \rho}{\partial t} + \overline{\rho}\frac{\partial u_r}{\partial r} + \frac{\mathrm{d}\overline{\rho}}{\mathrm{d}r}u_r + \frac{2}{r}\overline{\rho}u_r + \overline{\rho}\delta = 0, \tag{4.1}$$

with $\overline{\rho} = \lambda^n$. Here ξ is calculated based on the dominant eigenmode. Considering the symmetric structure of the dominant eigenmode, ξ is defined as

$$\xi = \frac{\left|\dfrac{\partial \rho}{\partial t}\right|_e}{\left|\dfrac{\partial \rho}{\partial t}\right|_e + \left|\overline{\rho}\dfrac{\partial u_r}{\partial r}\right|_e + \left|\dfrac{\mathrm{d}\overline{\rho}}{\mathrm{d}r}u_r\right|_e + \left|\dfrac{2}{r}\overline{\rho}u_r\right|_e + |\overline{\rho}\delta|_e}, \tag{4.2}$$

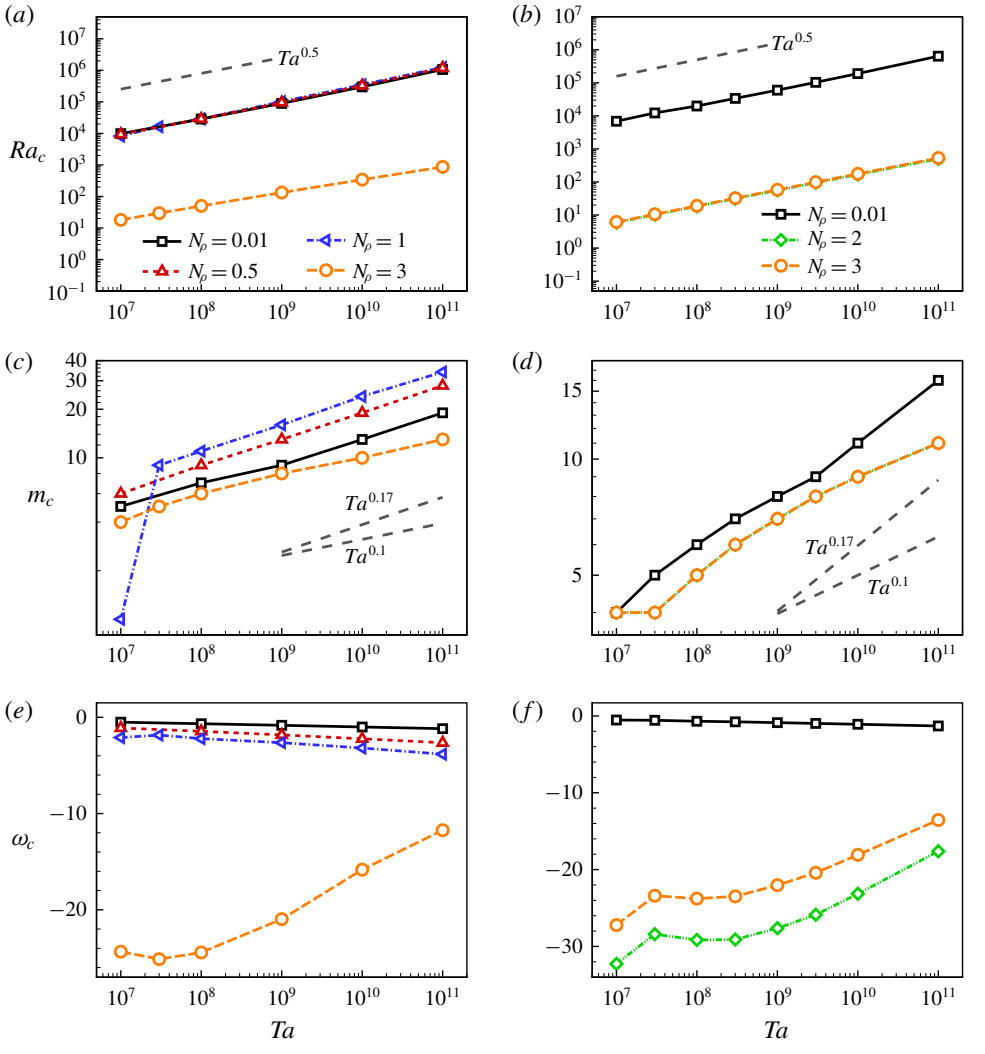

FIGURE 15. (Colour online) (*a*,*b*) Critical Rayleigh numbers Ra_c, (*c*,*d*) critical wavenumbers m_c and (*e*,*f*) critical frequencies ω_c as functions of Ta for different N_ρ at (*a*,*c*,*e*) $Pr = 0.3$ and (*b*,*d*,*f*) $Pr = 0.1$.

where $|f|_e$ is the maximum of $|f|$ on the equatorial plane and is used to measure the magnitude of f.

We consider the disturbance of wavenumber $m = 15$. Figure 17 shows the variations of ξ with Ra at $(Pr,\ Ta) = (0.1,\ 10^{10})$ and different N_ρ. It is observed that ξ is increased with the decrease of Ra, and the intensification of density stratification increases ξ significantly, indicating that the anelastic approximation is less applicable in the small-Ra and large-N_ρ regime. This is consistent qualitatively with the observations of rotating compressible convection in a plane layer geometry that, although the anelastic model can fail for marginally stable convection, it works well for supercritical convection at higher Ra (Verhoeven & Glatzmaier 2018). It is of

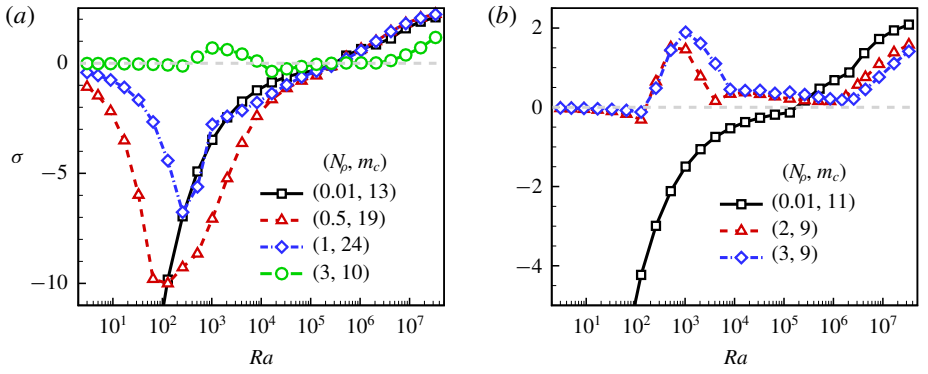

FIGURE 16. (Colour online) The maximal growth rates of the base state with respect to the disturbance of wavenumber $m = m_c(N_\rho)$ as functions of Ra at $Ta = 10^{10}$ and different values of N_ρ: (*a*) $Pr = 0.3$ and (*b*) $Pr = 0.1$.

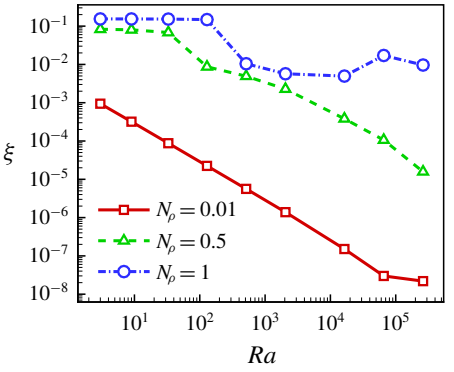

FIGURE 17. (Colour online) The relative magnitudes ξ of the time derivative of density perturbation in the continuity equation as functions of Ra at $(Pr, Ta) = (0.1, 10^{10})$ and different N_ρ.

interest to further examine the applicability of the anelastic model for small-Pr, rapidly rotating, compressible convection in the high-Ra cases.

In the following, the stability characteristics of the base state are considered in the small-Ra regime. The complex growth rate and disturbance magnitudes of the dominant eigenmode are obtained as functions of Ra. Considering the disturbance of wavenumber $m = 5$, the results for $Pr = 0.1$, $Ta = 10^6$ and $N_\rho = 4$ are shown in figure 18. It is found that the complex growth rate and disturbance magnitudes satisfy scaling laws with respect to Ra:

$$(\sigma, \omega, |u_r|_e, |u_\phi|_e) \sim O(Ra^{0.5}), \quad |p|_e \sim O(1), \quad |T|_e \sim O(Ra^1). \qquad (4.3a\text{–}c)$$

Normalization is employed for disturbance magnitudes such that $|\rho|_e = 1$. The scaling behaviours are universal with respect to parameters (Pr, Ta, N_ρ, m) in the small-Ra limit. By inspecting the disturbance out of the equatorial plane, it is found that u_θ is of the same order as u_r and u_ϕ.

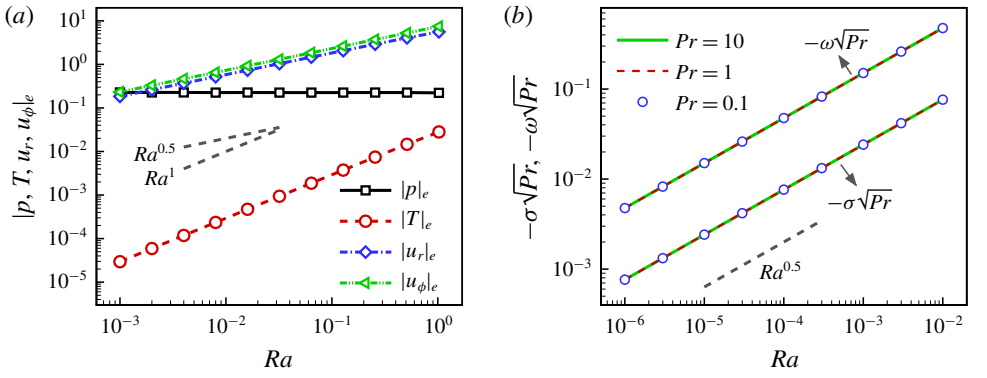

FIGURE 18. (Colour online) (*a*) Disturbance magnitudes and (*b*) complex growth rates of the dominant eigenmode of wavenumber $m = 5$ as functions of Ra in the small-Ra limit for $Ta = 10^6$, $N_\rho = 4$: (*a*) results for $Pr = 0.1$; and (*b*) variations of $-\sigma\sqrt{Pr}$ and $-\omega\sqrt{Pr}$ for $Pr = 10,\ 1,\ 0.1$.

Based on the scaling laws with Ra, the complex growth rate and disturbances are rescaled as

$$\tilde{\rho} = \rho, \quad (\tilde{\sigma}, \tilde{\omega}, \tilde{u}_r, \tilde{u}_\phi, \tilde{u}_\theta) = Ra^{-0.5}(\sigma, \omega, u_r, u_\phi, u_\theta), \quad \tilde{p} = p, \quad \tilde{T} = Ra^{-1}T. \tag{4.4a–d}$$

Using the rescaled quantities in the linear equations (2.9) and neglecting higher-order terms of Ra as $Ra \to 0$, we can scale Ra out of (2.9) and obtain

$$\left.\begin{gathered} \frac{\partial \tilde{\rho}}{\partial \tilde{t}} + \boldsymbol{\nabla}\cdot(\lambda^n \tilde{\boldsymbol{u}}) = 0, \\ \sqrt{Pr\,Ta}\,\lambda^n \hat{\boldsymbol{z}}\times\tilde{\boldsymbol{u}} + \frac{\boldsymbol{\nabla}\tilde{p}}{\epsilon} + \frac{\tilde{\rho}\boldsymbol{r}}{\epsilon(1-\eta)^2 r^3} = \sqrt{Pr}\left[\nabla^2\tilde{\boldsymbol{u}} + \frac{1}{3}\boldsymbol{\nabla}(\boldsymbol{\nabla}\cdot\tilde{\boldsymbol{u}})\right], \\ \lambda^n\,\tilde{\boldsymbol{u}}\cdot\boldsymbol{\nabla}\lambda + (\gamma-1)\lambda^{n+1}\boldsymbol{\nabla}\cdot\tilde{\boldsymbol{u}} = \frac{\gamma}{\sqrt{Pr}}\nabla^2\tilde{T}, \\ \lambda_b(n+1)(1-\eta)^2\tilde{p} = \lambda\tilde{\rho}. \end{gathered}\right\} \tag{4.5}$$

In the simplified equations (4.5), there is no time-derivative term in the momentum and temperature equations, while the time derivative of the density perturbation is non-negligible in the continuity equation. Thus, for specified ϵ or n, the anelastic approximation is inapplicable when Ra is small enough. We note that the decrease of $-\sigma$ in the small-Ra limit does not indicate that the base state becomes less stable. When the time scale is chosen appropriately in this limit, the rescaled growth rate $\tilde{\sigma}$, as shown in (4.4), approaches a finite negative value as $Ra \to 0$, indicating that the disturbance decays at a finite damping rate in the small-Ra limit.

In (4.5), the equation for temperature perturbation $\tilde{T}$ is decoupled from the other equations, and the density perturbation is directly related to the pressure perturbation. By some manipulations, a closed set of equations for $\tilde{\boldsymbol{u}}$ can be obtained:

$$\begin{aligned} &\sqrt{Pr}\frac{\partial}{\partial\tilde{t}}\left[\sqrt{Ta}\,\lambda^n\hat{\boldsymbol{z}}\times\tilde{\boldsymbol{u}} - \nabla^2\tilde{\boldsymbol{u}} - \frac{1}{3}\boldsymbol{\nabla}(\boldsymbol{\nabla}\cdot\tilde{\boldsymbol{u}})\right] \\ &\quad = \frac{1}{\epsilon\lambda_b(n+1)(1-\eta)^2}\boldsymbol{\nabla}[\lambda\boldsymbol{\nabla}\cdot(\lambda^n\tilde{\boldsymbol{u}})] + \frac{\boldsymbol{r}}{\epsilon(1-\eta)^2 r^3}\boldsymbol{\nabla}\cdot(\lambda^n\tilde{\boldsymbol{u}}). \end{aligned} \tag{4.6}$$

From (4.6) it is found that the rescaled complex growth rate $\tilde{\sigma} + \mathrm{i}\tilde{\omega}$ is proportional to $Pr^{-0.5}$ in the small-Ra limit. This is confirmed by linear stability analysis based on the full equations, as shown in figure 18(*b*). The distributions of velocity perturbations are independent of Pr. Since the coupling between thermal perturbations and velocity perturbations is dependent on Pr, the relative magnitudes of velocity perturbations with respect to thermal perturbations vary with Pr.

Overall, in the study of linear rotating compressible convection in a spherical shell, we demonstrate that the anelastic approximation becomes less applicable in the small-Ra and large-N_ρ regime. In the small-Ra limit the time derivative of the density perturbation is non-negligible, so that the anelastic model cannot be applied.

5. Summary

In this study, the stability characteristics of nearly adiabatic compressible convection in a rapidly rotating spherical shell are studied systematically by linear stability analysis based on the fully compressible Navier–Stokes equations, while the applicability of the anelastic approximation is also evaluated.

By investigating the stability characteristics of the base state with respect to the disturbance of specified wavenumber, it is found that the instability process is sensitive to Pr and to the intensity of density stratification. For large Pr and relatively weak density stratification, the columnar mode becomes unstable first; while for small Pr and strong density stratification, the new quasi-geostrophic compressible mode is identified, which loses stability first. The inertial mode can also occur first for small Pr and a certain intensity of density stratification. Although the critical Rayleigh numbers of the quasi-geostrophic compressible mode and columnar mode are different by several orders of magnitude, similar scaling behaviours of these critical quantities with Ta are observed.

Here, the critical Ra for convection onset is always positive, in contrast with previous results of the anelastic model that convection can occur at negative Ra. By measuring the relative magnitude of the time derivative of density perturbation in the continuity equation, it is found that the anelastic approximation is not suitable for the case with small Ra and large density stratification. When Ra is small enough, the complex growth rate and disturbance magnitudes satisfy certain scaling laws with Ra. In addition, we find that in the small-Ra limit the time derivative of the density perturbation is non-negligible, which limits the application of the anelastic model.

In this study, we focused on studying the linear stability characteristics of compressible convection in a rapidly rotating spherical shell based on the fully compressible equations and evaluated the applicability of the anelastic approximation. It is of interest to examine the applicabilities of other sound-proof approaches (Chenoweth & Paolucci 1986; Durran 2008; Verhoeven & Glatzmaier 2018) and to extend the linear analysis to the nonlinear regime to investigate the bifurcation nature of convection onset and fully nonlinear convection at higher Ra.

Acknowledgements

This work is supported by the National Natural Science Foundation of China (grant nos 11572314, 11621202, 11772323, U1730124), the Science Challenge Project (no. TZ2016001), and the Fundamental Research Funds for the Central Universities.

Appendix A

The terms $C_{r,\delta,\zeta}$ pertaining to the Coriolis force in the u_r, δ and ζ equations of (2.13) read

$$\left.\begin{aligned} C_r &= -\sqrt{\frac{Pr\,Ta}{Ra}}\lambda^n u_\phi \sin\theta, \\ C_\delta &= -\sqrt{\frac{Pr\,Ta}{Ra}}\lambda^n \left(-\frac{1}{r}\frac{\partial u_r}{\partial \phi} - \frac{u_\phi \sin\theta}{r} + \zeta\cos\theta\right), \\ C_\zeta &= \sqrt{\frac{Pr\,Ta}{Ra}}\lambda^n \left(\frac{\sin\theta}{r}\frac{\partial u_r}{\partial \theta} + \frac{2u_r\cos\theta}{r} - \frac{u_\theta\sin\theta}{r} + \delta\cos\theta\right). \end{aligned}\right\} \tag{A 1}$$

The terms $\tau_{r,\delta,\zeta}$ pertaining to the viscous force in (2.13) read

$$\left.\begin{aligned} \tau_r &= \sqrt{\frac{Pr}{Ra}}\left(\nabla^2 u_r + \frac{1}{3}\frac{\partial^2 u_r}{\partial r^2} + \frac{2}{3r}\frac{\partial u_r}{\partial r} - \frac{8u_r}{3r^2} + \frac{1}{3}\frac{\partial \delta}{\partial r} - \frac{2\delta}{r}\right), \\ \tau_\delta &= \sqrt{\frac{Pr}{Ra}}\left(\frac{1}{3}\frac{\partial}{\partial r}\nabla_H^2 u_r + \frac{10}{3r}\nabla_H^2 u_r + \frac{4}{3}\nabla^2\delta - \frac{1}{3}\frac{\partial^2\delta}{\partial r^2} + \frac{4}{3r}\frac{\partial\delta}{\partial r} + \frac{2\delta}{r^2}\right), \\ \tau_\zeta &= \sqrt{\frac{Pr}{Ra}}\left(\nabla^2\zeta + \frac{2}{r}\frac{\partial\zeta}{\partial r} + \frac{2}{r^2}\zeta\right). \end{aligned}\right\} \tag{A 2}$$

Appendix B

In the spherical harmonic expansion of a function $\chi(t, r, \theta, \phi)$ as shown in (2.16), the coefficients of spherical harmonics Y_l^m are χ_l^m. Below are some useful expressions for the expansion coefficients $[L\cdot\chi]_l^m$ of $L\cdot\chi$, where L is a linear operator:

$$\left.\begin{aligned} [\nabla_H^2\chi]_l^m &= -\frac{l(l+1)}{r^2}\chi_l^m, \\ [\nabla^2\chi]_l^m &= \left[\frac{\partial^2}{\partial r^2} + \frac{2}{r}\frac{\partial}{\partial r} - \frac{l(l+1)}{r^2}\right]\chi_l^m, \\ [\cos\theta\cdot\chi]_l^m &= c_{l+1}^m\chi_{l+1}^m + c_l^m\chi_{l-1}^m, \\ \left[\sin\theta\cdot\frac{\partial\chi}{\partial\theta}\right]_l^m &= (l-1)c_l^m\chi_{l-1}^m - (l+2)c_{l+1}^m\chi_{l+1}^m, \end{aligned}\right\} \tag{B 1}$$

where

$$c_l^m = \left(\frac{l^2-m^2}{4l^2-1}\right)^{1/2}. \tag{B 2}$$

We note that the expansion coefficients of terms containing u_θ and u_ϕ in (2.13) can be expressed in terms of the expansion coefficients of δ and ζ:

$$\left.\begin{aligned} [\sin\theta\cdot u_\theta]_l^m &= r\left[-\frac{c_l^m}{l}\delta_{l-1}^m + \frac{c_{l+1}^m}{l+1}\delta_{l+1}^m + \frac{\mathrm{i}m}{l(l+1)}\zeta_l^m\right], \\ [\sin\theta\cdot u_\phi]_l^m &= r\left[-\frac{c_l^m}{l}\zeta_{l-1}^m + \frac{c_{l+1}^m}{l+1}\zeta_{l+1}^m - \frac{\mathrm{i}m}{l(l+1)}\delta_l^m\right]. \end{aligned}\right\} \tag{B 3}$$

REFERENCES

BATCHELOR, G. K. 1953 The conditions for dynamical similarity of motions of a frictionless perfect-gas atmosphere. *Q. J. R. Meteorol. Soc.* **79** (340), 224–235.

BERKOFF, N. A., KERSALE, E. & TOBIAS, S. M. 2010 Comparison of the anelastic approximation with fully compressible equations for linear magnetoconvection and magnetic buoyancy. *Geophys. Astrophys. Fluid Dyn.* **104** (5–6), 545–563.

BRAGINSKY, S. I. & ROBERTS, P. H. 1995 Equations governing convection in Earth's core and the geodynamo. *Geophys. Astrophys. Fluid Dyn.* **79** (1–4), 1–97.

BROWN, B. P., VASIL, G. M. & ZWEIBEL, E. G. 2012 Energy conservation and gravity waves in sound-proof treatments of stellar interiors. Part I. Anelastic approximations. *Astrophys. J.* **756** (2), 109.

BUSSE, F. H. 1970 Thermal instabilities in rapidly rotating systems. *J. Fluid Mech.* **44** (3), 441–460.

BUSSE, F. H. & HOOD, L. L. 1982 Differential rotation driven by convection in a rapidly rotating annulus. *Geophys. Astrophys. Fluid Dyn.* **21** (1–2), 59–74.

BUSSE, F. H. & SIMITEV, R. 2004 Inertial convection in rotating fluid spheres. *J. Fluid Mech.* **498**, 23–30.

BUSSE, F. H., ZHANG, K. & LIAO, X. 2005 On slow inertial waves in the solar convection zone. *Astrophys. J. Lett.* **631** (2), L171–L174.

CAI, T., CHAN, K. L. & DENG, L. 2011 Numerical simulation of core convection by a multi-layer semi-implicit spherical spectral method. *J. Comput. Phys.* **230** (24), 8698–8712.

CALKINS, M. A., JULIEN, K. & MARTI, P. 2015*a* The breakdown of the anelastic approximation in rotating compressible convection: implications for astrophysical systems. *Proc. R. Soc. Lond.* A **471** (2175), 20140689.

CALKINS, M. A., JULIEN, K. & MARTI, P. 2015*b* Onset of rotating and non-rotating convection in compressible and anelastic ideal gases. *Geophys. Astrophys. Fluid Dyn.* **109** (4), 422–449.

CHAN, K. L., MAYR, H. G., MENGEL, J. G. & HARRIS, I. 1994 A 'stratified' spectral model for stable and convective atmospheres. *J. Comput. Phys.* **113** (2), 165–176.

CHANDRASEKHAR, S. 1961 *Hydrodynamic and Hydromagnetic Stability*. Clarendon Press.

CHENOWETH, D. R. & PAOLUCCI, S. 1986 Natural convection in an enclosed vertical air layer with large horizontal temperature differences. *J. Fluid Mech.* **169**, 173–210.

DORMY, E., SOWARD, A. M., JONES, C. A., JAULT, D. & CARDIN, P. 2004 The onset of thermal convection in rotating spherical shells. *J. Fluid Mech.* **501**, 43–70.

DREW, S. J., JONES, C. A. & ZHANG, K. 1995 Onset of convection in a rapidly rotating compressible fluid spherical shell. *Geophys. Astrophys. Fluid Dyn.* **80** (3–4), 241–254.

DURRAN, D. R. 2008 A physically motivated approach for filtering acoustic waves from the equations governing compressible stratified flow. *J. Fluid Mech.* **601**, 365–379.

GILMAN, P. A. & GLATZMAIER, G. A. 1981 Compressible convection in a rotating spherical shell. I. Anelastic equations. *Astrophys. J. Suppl.* **45**, 335–349.

GLATZMAIER, G. A. & GILMAN, P. A. 1981*a* Compressible convection in a rotating spherical shell. II. A linear anelastic model. *Astrophys. J. Suppl.* **45**, 351–380.

GLATZMAIER, G. A. & GILMAN, P. A. 1981*b* Compressible convection in a rotating spherical shell. IV. Effects of viscosity, conductivity, boundary conditions, and zone depth. *Astrophys. J. Suppl.* **47**, 103–115.

GUILLOT, T. 1999*a* A comparison of the interiors of Jupiter and Saturn. *Planet. Space Sci.* **47** (10–11), 1183–1200.

GUILLOT, T. 1999*b* Interiors of giant planets inside and outside the solar system. *Science* **286** (5437), 72–77.

JONES, C. A., BORONSKI, P., BRUN, A. S., GLATZMAIER, G. A., GASTINE, T., MIESCH, M. S. & WICHT, J. 2011 Anelastic convection-driven dynamo benchmarks. *Icarus* **216** (1), 120–135.

JONES, C. A., KUZANYAN, K. M. & MITCHELL, R. H. 2009 Linear theory of compressible convection in rapidly rotating spherical shells, using the anelastic approximation. *J. Fluid Mech.* **634**, 291–319.

JONES, C. A., ROBERTS, P. H. & GALLOWAY, D. J. 1990 Compressible convection in the presence of rotation and a magnetic field. *Geophys. Astrophys. Fluid Dyn.* **53** (3), 145–182.

JONES, C. A., ROTVIG, J. & ABDULRAHMAN, A. 2003 Multiple jets and zonal flow on Jupiter. *Geophys. Res. Lett.* **30** (14), 1731.

JONES, C. A., SOWARD, A. M. & MUSSA, A. I. 2000 The onset of thermal convection in a rapidly rotating sphere. *J. Fluid Mech.* **405**, 157–179.

LECOANET, D., BROWN, B. P., ZWEIBEL, E. G., BURNS, K. J., OISHI, J. S. & VASIL, G. M. 2014 Conduction in low Mach number flows. I. Linear and weakly nonlinear regimes. *Astrophys. J.* **797** (2), 94.

LUND, T. S. & FRITTS, D. C. 2012 Numerical simulation of gravity wave breaking in the lower thermosphere. *J. Geophys. Res.* **117** (D21), D21105.

OGURA, Y. & PHILLIPS, N. A. 1962 Scale analysis of deep and shallow convection in the atmosphere. *J. Atmos. Sci.* **19** (2), 173–179.

PROUDMAN, J. 1916 On the motion of solids in a liquid possessing vorticity. *Proc. R. Soc. Lond.* A **92** (642), 408–424.

ROBERTS, P. H. 1968 On the thermal instability of a rotating-fluid sphere containing heat sources. *Phil. Trans. R. Soc. Lond.* A **263** (1136), 93–117.

ROTVIG, J. & JONES, C. A. 2006 Multiple jets and bursting in the rapidly rotating convecting two-dimensional annulus model with nearly plane-parallel boundaries. *J. Fluid Mech.* **567**, 117–140.

SÁNCHEZ, J., GARCIA, F. & NET, M. 2016*a* Critical torsional modes of convection in rotating fluid spheres at high Taylor numbers. *J. Fluid Mech.* **791**, R1.

SÁNCHEZ, J., GARCÍA, F. & NET, M. 2016*b* Radial collocation methods for the onset of convection in rotating spheres. *J. Comput. Phys.* **308**, 273–288.

SPIEGEL, E. A. & VERONIS, G. 1960 On the Boussinesq approximation for a compressible fluid. *Astrophys. J.* **131**, 442–447.

TAKEHIRO, S. 2008 Physical interpretation of spiralling-columnar convection in a rapidly rotating annulus with radial propagation properties of Rossby waves. *J. Fluid Mech.* **614**, 67–86.

TAKEHIRO, S. 2010 Kinetic energy budget analysis of spiraling columnar critical convection in a rapidly rotating spherical shell. *Fluid Dyn. Res.* **42** (5), 055501.

TAYLOR, G. I. 1921 Experiments with rotating fluids. *Proc. R. Soc. Lond.* A **100** (703), 114–121.

TREFETHEN, L. N. 2000 *Spectral Methods in MATLAB*. SIAM.

VERHOEVEN, J. & GLATZMAIER, G. A. 2018 Validity of sound-proof approaches in rapidly-rotating compressible convection: marginal stability versus turbulence. *Geophys. Astrophys. Fluid Dyn.* **112** (1), 36–61.

VERHOEVEN, J., WIESEHÖFER, T. & STELLMACH, S. 2015 Anelastic versus fully compressible turbulent Rayleigh–Bénard convection. *Astrophys. J.* **805** (1), 62.

YANO, J.-I. 1992 Asymptotic theory of thermal convection in rapidly rotating systems. *J. Fluid Mech.* **243**, 103–131.

ZHANG, K. 1992 Spiralling columnar convection in rapidly rotating spherical fluid shells. *J. Fluid Mech.* **236**, 535–556.

ZHANG, K. 1994 On coupling between the Poincaré equation and the heat equation. *J. Fluid Mech.* **268**, 211–229.

ZHANG, K. 1995 On coupling between the Poincaré equation and the heat equation: non-slip boundary condition. *J. Fluid Mech.* **284**, 239–256.

ZHANG, K. & BUSSE, F. H. 1987 On the onset of convection in rotating spherical shells. *Geophys. Astrophys. Fluid Dyn.* **39** (3), 119–147.

ZHANG, K., LAM, K. & KONG, D. 2017 Asymptotic theory for torsional convection in rotating fluid spheres. *J. Fluid Mech.* **813**, R2.

ZHANG, K. & LIAO, X. 2017 *Theory and Modeling of Rotating Fluids: Convection, Inertial Waves and Precession*. Cambridge University Press.